High-Performance Quantum-Dot Solids via Elemental Sulfur Synthesis

*Mingjian Yuan, Kyle W. Kemp, Susanna M. Thon, Jin Young Kim, Kang Wei Chou, Aram Amassian, and Edward H. Sargent**

PbS colloidal quantum dots (CQDs) are attractive materials for use in photovoltaic applications due to their facile solution processing,[1,2] their potential for efficient multiple exciton generation and harvesting,[3] and their spectral tunability based on the quantum-size-effect.[4] Since the report of the first PbS CQD solar cell in 2005,[5] rapid progress in CQD photovoltaic device architectures and improvements in electronic material properties have led to certified AM 1.5 solar power conversion efficiencies of 7%.[6–8]

One of the main advantages of using quantum confined nanostructures for photovoltaics is their potential for deployment in multijunction solar cells.[9] In a multijunction cell, semiconductors with different bandgaps sequentially extract power from their respective portions of the sun's broad spectrum. In principle, these devices can lead to higher solar-power conversion efficiencies compared with traditional single-junction devices.[1] However, the difficulty of tuning the bandgaps of chemically compatible semiconductor materials has rendered traditional epitaxial multijunction cells more difficult and expensive to produce than traditional single-junction devices.

CQDs have the potential to solve this problem by enabling layers with different bandgaps, programmed via quantum size-effect tuning, to be fabricated using a single materials processing strategy. Recently, a proof-of-principle tandem photovoltaic device based on PbS CQDs was demonstrated[9] with the front and back cells employing 1.6 eV and 1.0 eV bandgap CQDs, respectively. The performance of the tandem device was limited by the back cell based on the larger CQDs. CQDs possessing smaller bandgaps should allow for broader solar absorption, thereby enabling higher currents; however, limitations in synthesis and processing strategies of larger CQDs have kept the record power conversion efficiency of 1.0 eV bandgap PbS CQDs solar cells at 3.8%.[10] This is attributed to the difficulty in fully passivating the surfaces of larger CQDs during processing steps, and to larger size dispersions of large-diameter CQD ensembles following synthesis.[11]

High performance and low materials cost will be required simultaneously for a competitive PbS-CQD-based technology. This provides further impetus to develop improved processing and growth paradigms with low cost syntheses of larger-diameter PbS CQDs.

The conventional synthesis method for high-quality PbS CQDs is based on a highly reactive sulfur source,[12] bis (trimethylsilyl) sulfide (TMS_2S). The use of TMS_2S provides a fast reaction, yielding PbS CQDs with a relatively narrow size distribution. To date, all published performance records for optoelectronic devices based on PbS CQDs have relied on the TMS_2S synthesis.[8] However, TMS_2S is both pyrophoric and expensive. The TMS_2S source accounts for over 80% of the PbS CQDs synthesis materials cost, limiting the potential for low-cost scale-up of the synthesis and, by extension, the widespread deployment of technologies based on PbS CQDs. Furthermore, the method results in relatively high polydispersity for small bandgap CQDs due to the high reactivity of TMS_2S.[13]

For these reasons, we seek herein to address the need for a scalable, low-cost synthetic path to high-quality PbS CQDs with small bandgaps by developing an improved synthesis and processing protocol for 1 eV bandgap dots.

Our synthetic approach was based on lead chloride ($PbCl_2$) and elemental sulfur (S) in oleylamine (OLA) as the precursors. Elemental sulfur-oleylamine solutions exist mainly as alkylammonium polysulfides.[14] Upon heating to the temperatures required for nanocrystal growth, the polysulfide ions react with excess oleylamine to liberate H_2S, which combines with the $PbCl_2$ precursor to form PbS CQDs.[15] Elemental-sulfur-based synthesis procedures have been used to produce small bandgap CQDs in the past;[16] however, they involve several practical disadvantages, including poor air stability and a wide size distribution associated with imperfect surface passivation. As a result, no optoelectronic device data based on the elemental sulfur precursor synthesis of PbS CQDs have been reported to date.

We took the view that elemental-sulfur-based synthesis, combined with novel processing techniques to improve size dispersity and passivation, could result in a low-cost high-quality platform for smaller bandgap PbS-CQD-based devices. We used size-selective precipitation and cadmium chloride passivation to dramatically improve the power conversion efficiencies of 1 eV PbS CQD photovoltaic devices. Our method resulted in

Dr. M. Yuan, Dr. K. M. Kemp, Dr. S. M. Thon, Dr. J. Y. Kim, Prof. E. H. Sargent
Department of Electrical and Computer Engineering
University of Toronto
10 King's College Road,
Toronto, Ontario M5S 3G4, Canada
E-mail: ted.sargent@utoronto.ca
Dr. S. M. Thon
Department of Electrical and Computer Engineering
Johns Hopkins University
Baltimore, Maryland 21218, USA
Dr. J. Y. Kim
Fuel Cell Research Center
Korea Institute of Science and Technology (KIST)
Seoul 136–791, South Korea
Dr. K. W. Chou, Prof. A. Amassian
Physical Sciences and Engineering Division, Solar and Photovoltaic Engineering Research Center
King Abdullah University of Science and Technology (KAUST)
Thuwal 23955–6900, Saudi Arabia

DOI: 10.1002/adma.201305912

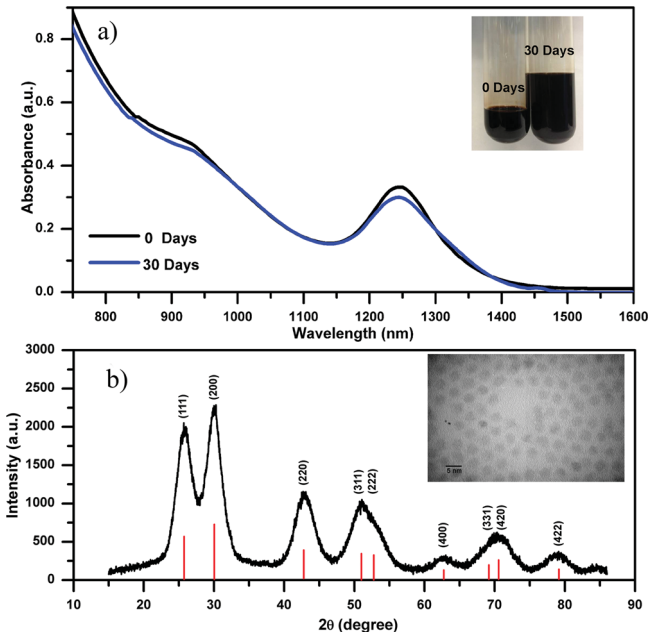

Figure 1. a) Absorption spectra of the as-synthesized PbS CQDs in toluene (black line) and the absorption spectra of the as-synthesized PbS CQD solutions stored for 30 days in air (blue line). b) XRD spectrum of a PbS CQD film. The standard diffraction pattern (JCPDS 02–0699) for bulkPbS is indicated by the red lines; the inset shows a STEM image of the PbS CQDs.

high-quality, monodisperse CQD solutions and a record power conversion efficiency for a 1 eV PbS CQD solar cell of 5.4%.

Our synthesis procedure began with heating a solution of $PbCl_2$ and OLA to 80 °C under nitrogen. According to previous reports,[15] solutions of $PbCl_2$ in OLA result in a heterogeneous system and form a turbid suspension. Previous work has suffered from the inability to isolate highly pure CQDs from the insoluble $PbCl_2$ particles in the reaction mixtures. However, we found that the viscosity of the growth environment could be tuned by varying the $PbCl_2$:OLA ratio. By increasing the amount of OLA, a homogeneous yellowish solution could be produced instead of the turbid suspension. CQD growth was then triggered by hot-injection of a sulfur-OLA solution.

As seen in **Figure 1**a, our as-synthesized PbS CQDs showed a well-defined excitonic absorption peak centered at 1245 nm with a full width at half-maximum (FWHM) of 103 nm. They exhibited strong photoluminescence in the near infrared with a solution-phase photoluminescence quantum yield (PLQY) of 47 ± 5%. We imaged the CQDs using scanning transmission electron microscopy (STEM) as shown in the inset of Figure 1b. The average diameter of the PbS CQDs was 4.0 ± 0.5 nm, in agreement with the model proposed by Moreels:[17]

$$E_0 = 0.41 + (0.0252d^2 + 0.283d)^{-1} \quad (1)$$

where E_0 and d are the bandgap and diameter of the PbS nanocrystals respectively.

Powder X-ray diffraction (XRD) was employed to investigate the crystal structure of the CQDs. The position of the diffraction peaks (Figure 1b) matched the standard diffraction pattern for face-centered cubic PbS (JCPDS 02–0699), which confirmed that the CQDs synthesized using the elemental sulfur precursor were single-phase PbS. The mean domain size, which is equivalent to the nanocrystal size, was determined through Rietveld refinement of the XRD data. The mean domain size was found to be 4.1 ± 0.3 nm, consistent with the CQD size measured via STEM imaging. X-ray-photoelectron spectroscopy (XPS) and inductively coupled plasma atomic emission spectroscopy (AES-ICP) confirmed that the CQDs as-synthesized were Pb-rich with an average atomic ratio (Pb:S) of 1.6 ± 0.1. Charge balance was provided by Cl^- ions adsorbed on the surface, which were determined by XPS and ICP to be present in an atomic percentage of 30% relative to Pb.

We also investigated the colloidal stability of the elemental sulfur precursor synthesis CQDs. In the as-synthesized CQDs, the OLA weakly coordinates to the surface Pb atoms through lone nitrogen pairs. We observed that the initially transparent solutions changed into turbid suspensions after several hours, indicating a loss of ligands and subsequent PbS CQD agglomeration. To solve this problem, we performed a solution-phase ligand exchange. Due to the dynamic nature of the OLA ligands, the OLA could be exchanged for oleic acid (OA) which bonds more strongly to Pb and significantly improved stability. Figure 1a compares the absorption spectrum of a freshly prepared PbS CQD solution with the spectrum after 1 month. The absence of any significant changes indicates that the ligands are unperturbed during storage.

We built solar cells employing the depleted heterojunction architecture[18] out of our 1 eV-bandgap elemental sulfur precursor synthesis CQDs. We experimentally measured the band alignment of the PbS CQD films using cyclic voltammetry and absorption measurements. We used a calibrated $Ag/AgNO_3$ reference electrode with an electrode potential of 4.7 eV relative to vacuum. We measured the CQD film conduction band to lie at −4.0 eV, from which we calculated a valence band position of −5.0 eV using the optical bandgap.

In the depleted heterojunction architecture, the shallower conduction band edge energy of the CQD film provides a driving force for electron injection from the p-type CQD film to the conduction band of the n-type wide bandgap TiO_2 electrode. We employed sputtered TiO_2 with an electron affinity of −4.2 eV, thus providing a 0.2 eV conduction band offset.[19] We used a layer-by-layer spin-casting process to build the CQD film. The fabrication protocol for each layer consisted of three steps: deposition of CQDs dispersed in octane, followed by a mercaptopropionic acid in methanol ligand exchange, followed by a methanol rinse (see Methods for details). This process was repeated ten times to produce films of approximately 300 nm thickness. Molybdenum trioxide, gold and silver were then deposited on top of the film to contact the device. The current density–voltage (J–V) characteristics of a representative device under 100 mW cm^{-2} AM 1.5G simulated irradiation are shown in **Figure 2**. The device exhibited a short-circuit current (J_{SC}) density of 17.1 mA/cm^2, an open circuit voltage (V_{OC}) of 0.35 V, and a fill factor (FF) of 41.3%. The maximum power conversion efficiency was 2.5%.

Based on our initial device characterization, we determined that the following two factors limited device performance. A high density of electronic trap states is known in PbS CQDs

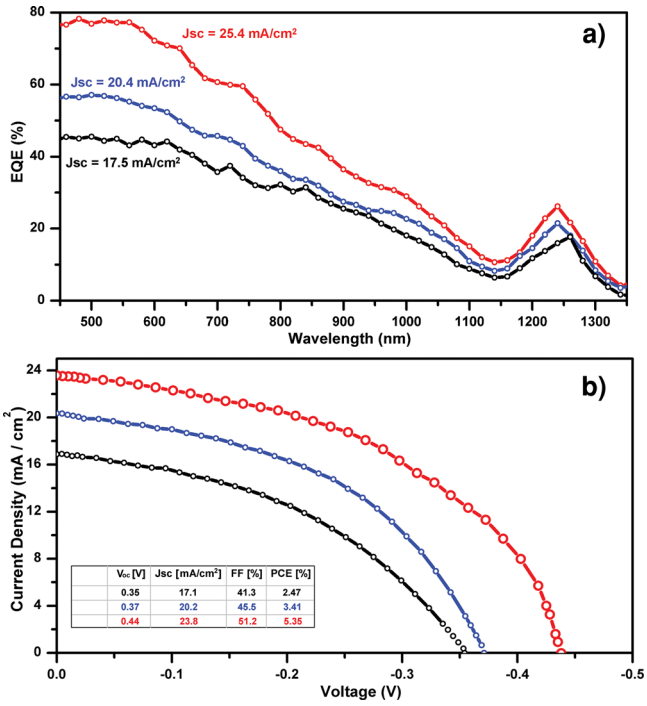

Figure 2. EQE spectra (a) and *J–V* curves (b) of the solar cells based on different PbS CQD films: as-synthesized (black), after size-selective precipitation (blue), and after size-selective precipitation plus metal halide treatment (red).

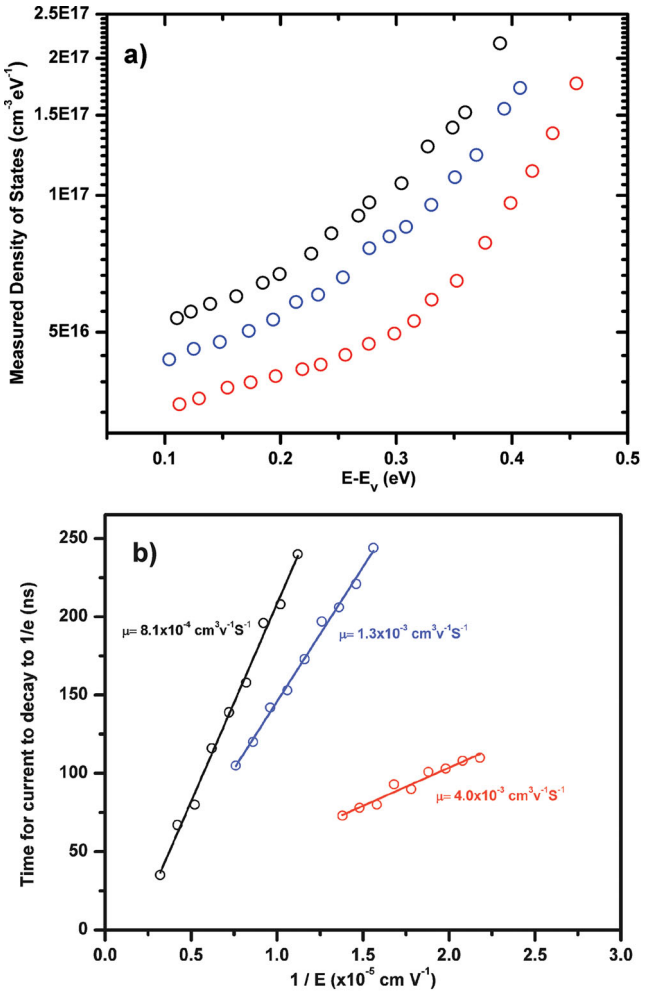

Figure 3. a) Density of trap states in the bandgap calculated from transient photovoltage measurements for as-synthesized (black), after size-selective precipitation (blue), and after size-selective precipitation plus metal halide treatment (red) PbS CQD films. b) Extracted carrier mobility calculated from transient photocurrent measurements for different PbS CQD films.

films to arise from suboptimal nanoparticle growth or ligand exchange during film fabrication.[20] Trap states militate against efficient charge extraction from CQDs films, even when present at small concentrations, and also lead to non-radiative recombination pathways that lower open circuit voltage.[21,22] Previous studies have shown that a high density of electronic trap states will significantly reduce the power conversion efficiency of a photovoltaic device.[23] Secondly, poor charge carrier mobility can also limit performance: typical carrier lifetimes in CQD films are on the order of microseconds in the best cases, and minority carriers need to be extracted over distances on the order of hundreds of nanometers. For this reason, improved charge carrier mobility in CQD films, ideally reaching well above 0.01 $cm^2\ V^{-1}\ s^{-1}$, is prized in realizing high-performance CQD solar cells.[24]

We sought experimental evidence of the origins of relatively low device performance, turning to transient photovoltage and photocurrent spectroscopy to investigate the trap state density and the charge-carrier mobility, respectively, of the as-synthesized 1 eV PbS CQD solids.

The density of electronic trap states was obtained using the photovoltage transient method.[25,26] This method can probe the photogenerated filling of midgap levels. An 830 nm diode laser provided a constant light bias, and a pulsed 640 nm diode laser modulated the V_{OC}. By measuring the change in V_{OC} and the total generated charge for each perturbation across a wide range of light bias intensities, we were able to extract the density of trap states as a function of energetic depth within the bandgap of the quantum-dots solid. As shown in **Figure 3**, we measured the average density of trap states to be $(9 \pm 0.4) \times 10^{16}\ cm^{-3}\ eV^{-1}$ at an energy level near the middle of the bandgap in our 1 eV PbS CQD solid. This value is fully an order of magnitude higher than in state-of-the-art PbS CQD photovoltaic films. The high density of trap states increases the rate of carrier recombination, decreases the charge carrier extraction efficiency, and produces a smaller V_{OC} and lower J_{SC} than could be achieved in an optimized film.

In order to measure the charge-carrier mobility, we used the photocurrent transient method.[27] A 640 nm pulsed diode laser with an illumination intensity set to approximately 1 sun excited photocarriers in the device. Effective transit times (the time for current to decay to $1/e$ of the peak value) were obtained as a function of device bias. With knowledge of the film thickness, we used transit time versus average field to extract the limiting carrier mobility. Transient short current spectroscopy is used to measure the drift mobility of the limiting carrier type. We measured our as-synthesized film to have an average electron mobility μ_e of $(8.1 \pm 0.2) \times 10^{-4}\ cm^2\ V^{-1}\ s^{-1}$. Previous reports

have shown that the mobility must exceed approximately 1.0×10^{-3} cm^2 V^{-1} s^{-1} to achieve optimal device performance.[18]

As discussed, the optimization efforts need to concentrated on eliminating electronic states detrimental to carrier lifetime and improving charge carrier mobility to get better carrier extraction. Hence, we decided to address two common causes of trap states in colloidal-quantum-dot films, nanocrystal size polydispersity and incomplete surface passivation, by developing two post-synthesis processing procedures in parallel.[21]

When employed as a photovoltaic material, a CQD solid must be strongly electronically coupled, which is facilitated in part by minimizing the nanocrystal spacing, enhancing charge carrier mobility. In addition, it is desirable to eliminate chemical impurities to avoid formation of deep electronic trap states. Hence, the need for control over CQD population inhomogeneous broadening is widely recognized in the community.[28] In light-emitting devices, polydispersity widens the emission bandwidth. In electronic devices such as field-effect transistors, electronic transport can be enhanced through the use of highly monodispersed quantum dots, enabling dense packing and, potentially, superlattice-based delocalized transport. Polydispersity not only impedes transport but also can create "quantum traps", in which the presence of a small-bandgap inclusion produces enhanced recombination.[29] We decided to remedy polydispersity in our CQD materials by employing size-selective precipitation.

Gradual addition of a nonsolvent can produce size-dependent flocculation of the QD dispersion. This phenomenon can be exploited to further narrow the particle size distribution. **Figure 4** illustrates the result of size-selective precipitation. The optical absorption of the initial growth solution is shown in Figure 1a. The broad absorption features correspond to a sample with an average size of 40 Å ± 10% (sized by TEM, Figure 4a-b). Slow addition of ethanol results in the flocculation of the larger particles in the distribution which result in the spectrum shown in Figure S3 in the Supporting Information. The new solution has particles with an average size of 38 Å ± 5% (Figure 4c-d). The spectrum (Figure S3) is dramatically sharpened and blue-shifted relative to that of the as-synthesized growth solution. This reveals that the polydispersity and average particle size were reduced as a result of size-selective precipitation.[32]

Transient photovoltage spectroscopy was used to obtain the midgap trap state density inside the monodisperse film. The density was found to be $(6 \pm 0.6) \times 10^{16}$ cm^{-3} eV^{-1}, fully one and half times lower than in the as-synthesized films. An enhanced electron mobility of $\mu_e = (1.3 \pm 0.1) \times 10^{-3}$ cm^2 V^{-1} s^{-1}, was also observed for the films made using the more monodispersed dots. As expected, we found that the monodispersed CQDs showed improved performance resulting in a power conversion efficiency of 3.4%. The main improvement seen in the devices based on the size-selective precipitation step was an increase in the current and fill factor compared to the as-synthesized devices.

In addition to polydispersity, we addressed the issue of incomplete surface passivation of our CQDs. As discussed, reducing the trap state energy depth and volume density represents one of the most important ways to improve the transport properties, performance, and stability of CQD photovoltaic films.[30,31] Recently, a robust hybrid passivation strategy which involves introducing halide anions and metal cations during the synthesis was shown to be effective at removing surface

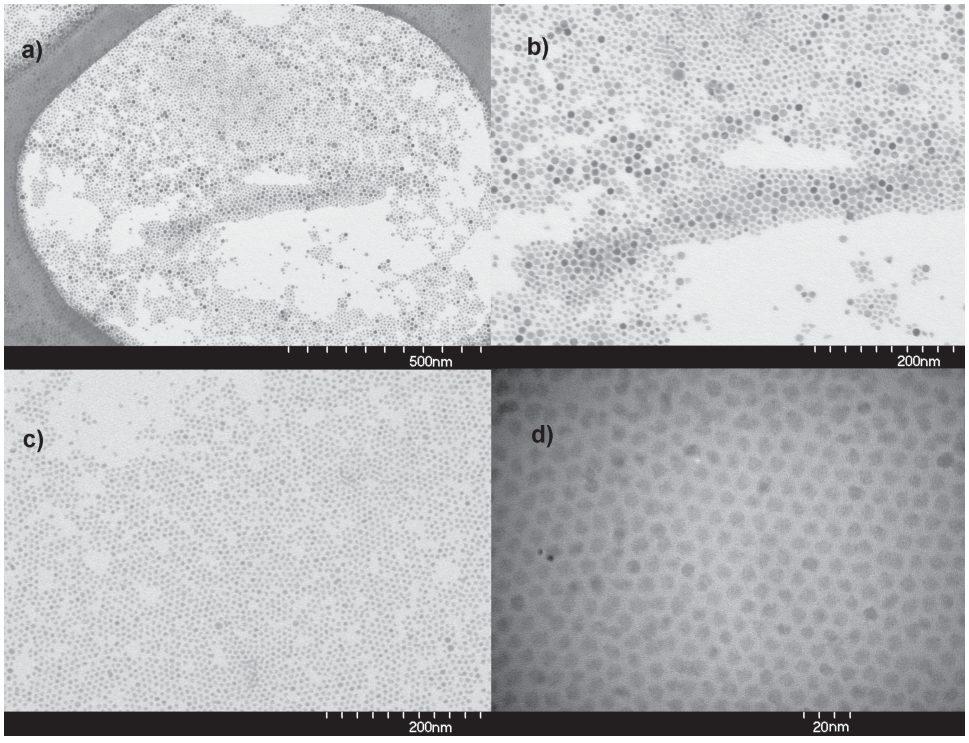

Figure 4. TEM images of the as-synthesized PbS CQDs (a,b) and PbS CQDs after size-selective precipitation (c,d)

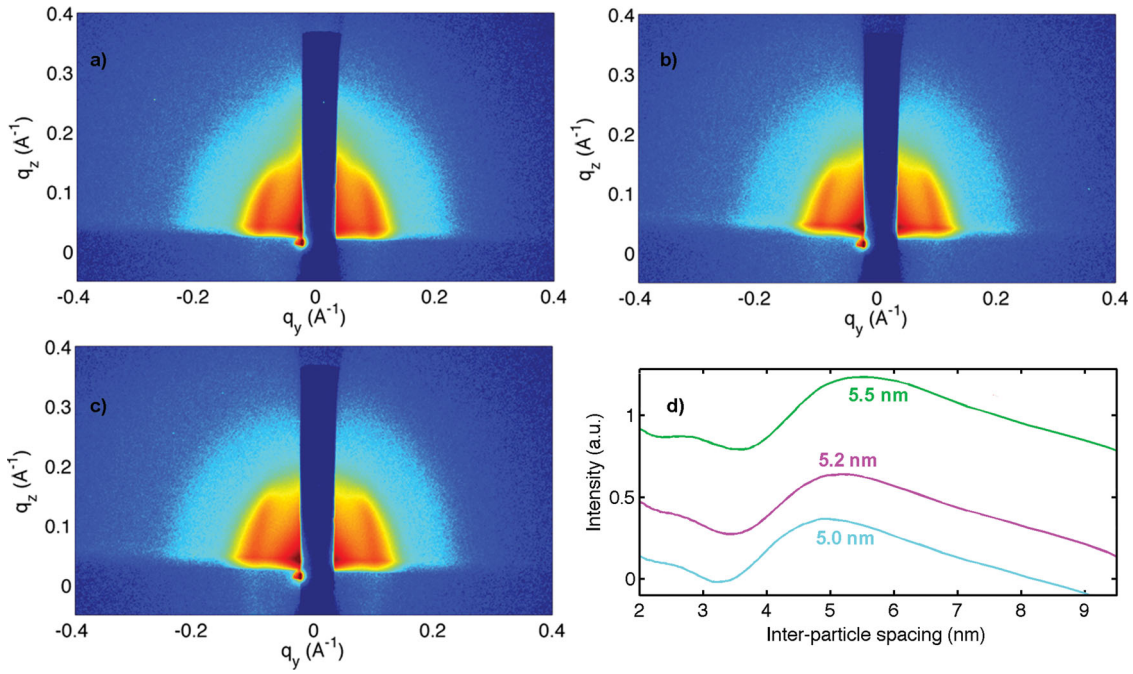

Figure 5. GISAXS intensity patterns of an as-cast, as synthesized PbS CQD film (a), a film composed of PbS CQDs after size-selective precipitation (b) and a film composed of PbS CQDs after size-selective precipitation plus metal halide treatment (c). The axes represent the scattering wave vectors in the plane of the substrate, $q_{x,y}$ (scattering in the plane of the substrate) and in the z direction, q_z (scattering normal to the plane of the substrate), respectively. The color scale represents the log of the scattering intensity as recorded by the CCD detector. Blue represents lower intensity and red represents higher intensity, with each spectrum normalized to show the full dynamic range of each data set. d) By integrating the intensity in a–c azimuthally, the average interparticle spacing can be found for the as synthesized PbS CQD film (green curve), PbS CQD film after size-selective precipitation (pink curve) and PbS CQD film after size-selective precipitation plus metal halide treatment (cyan curve).

trap states within the bandgap.[6,23] Metal cations have been reported to incorporate by binding to exposed sulfur atoms on the CQD surfaces in submonolayer quantities. The halide ions are able to passivate sites that organic ligands are unable to reach in light of steric hindrance or unfavorable surface topology, thereby improving passivation and reducing the density of electronic trap states.

We applied the hybrid passivation strategy to our new synthesis procedure in order to further reduce the trap state density in our CQD films. XPS and ICP-AES analysis indicated that introduction of the $CdCl_2$ solution immediately following the nucleation and growth of the CQDs did not result in the incorporation of the added passivants, probably due to the different reaction kinetics in our elemental-sulfur-precursor-based synthesis. We instead introduced $CdCl_2$ in a mixture of tetradecylphosphonic acid (TDPA) and oleylamine after the synthesis and initial isolation step. As confirmed by XPS and ICP-AES, the halide and Cd^{2+} bound to excess surface atoms while displacing a fraction of the oleic acid. Transient photovoltage spectroscopy was used to obtain the midgap trap state density inside the hybrid passivated film. The density was found to be $(3 \pm 0.2) \times 10^{16}$ cm^{-3} eV^{-1}, fully two times lower than the monodispersed-dot films that did not employ the passivation enhancement strategy. An enhanced electron mobility of $\mu_e = (4.0 \pm 0.3) \times 10^{-3}$ cm^2 V^{-1} s^{-1} was also observed for the films after the passivation post-treatment. As expected, we found that the device made from the CQDs employing both size-selective precipitation and passivation enhancement showed improved performance including a power conversion efficiency of 5.4%. We also simulated optoelectronic device performance of prospective CQD tandem cells employing the improved 1 eV PbS CQDs (Figure S1, S2, Supporting Information) in the back cell. The results show that 7% power conversion efficiency can realistically be achieved with the improved dots.

Additionally, we performed synchrotron-based grazing-incidence small-angle X-ray scattering (GISAXS) measurements (see Experimental Section) to look at the structure of films made with the different types of PbS CQDs (**Figure 5**). We determined that there was a statistically significant difference in the average interparticle spacing in the three cases (Figure 5d). The films made from as-synthesized CQDs, CQDs after size-selective precipitation, and CQDs after both size-selective precipitation and metal halide treatment had average spacings of 5.5 nm, 5.2 nm, and 5.0 nm, respectively. By improving monodispersity, selective precipitation facilitated the improved average center-to-center nanocrystal spacing reduction from 5.5 nm to 5.2 nm. The additional impact on dot spacing that comes from halide passivation may arise from the partial displacement of oleic acid ligands by chloride ions during the solution-phase halide treatment. When films are then formed in preparation for subsequent solid-statement treatment with the crosslinker MPA, these precursor films are more closely packed in light of their lower organic content. The ensuing solid-state exchange then also less disruptive to packing since it involves the removal of a smaller volume of oleic acid. These factors combined can account for the final further reduction in dot spacing to 5.0 nm

for the size-selectively precipitated, halide-treated, films. The finding confirms that the combination of post-synthesis treatment strategies leads to closely packed, homogeneous films.

In conclusion, we have demonstrated a low-cost synthetic method to produce 1eV PbS CQDs using an elemental sulfur precursor. Our method also involves size-selective precipitation and hybrid passivation to produce low-trap-state-density CQD films and resulted in a record solar power conversion efficiency of 5.4% for a 1 eV CQD photovoltaic cell. The method provides a general strategy for optimizing a scalable CQD synthesis system for high-performing optoelectronic films.

Experimental Section

PbS CQD Synthesis: 843 mg (3 mmol) of $PbCl_2$ was mixed with 12.5 mL of oleylamine in a Schlenk flask. The mixture was degassed for 30 min at 120 °C. $PbCl_2$ was fully dissolved in oleylamine, and a viscous transparent solution of slightly yellow color formed after heating. Meanwhile, a stock solution was prepared by mixing 160 mg of elemental sulfur and 15 mL of oleylamine which was heated to 125 °C for 30 min under nitrogen. The $PbCl_2$ solution was then cooled to the required injection temperature of 80 °C. The homogeneous $PbCl_2$ solution was stable at 80 °C and no $PbCl_2$ white precipitate was observed during the cooling process. Then, 2.25 mL of OLA-S stock solution was injected into the system, and the reaction temperature was stabilized at 80 °C for the PbS CQD growth. After 20 min, the reaction was quenched by adding 15 mL of toluene and 20 mL of ethanol. After centrifugation of the suspension and decantating of the supernatant, the CQDs were redispersed in 5 mL of toluene and passed through a 200 nm filter (Information regarding the $PbCl_2$-OLA solution, $PbCl_2$ solubility, $PbCl_2$ particle size, and ability to separate PbS nanocrystals from the $PbCl_2$ precursor as a function of the temperature and $PbCl_2$:OLA ratio, are provided in Table S1 in the Supporting Information).

Ligand Exchange: The oleylamine ligands were replaced by adding oleic acid to a CQDs toluene solution (40 mg/mL) in a ratio of 1:5 oleic acid:toluene. After precipitation with ethanol and centrifugation, the CQDs were redispersed in toluene, and the exchange was repeated. Finally, the CQDs were precipitated with ethanol to remove excess oleic acid.

Size-Selective Precipitation: As-synthesized PbS CQDs weredispersed in anhydrous toluene at 150 mg mL^{-1}. Anhydrous ethanol was then added dropwise to the dispersion until solid precipitation appeared. Separation of supernatant from the flocculate was achieved by centrifugation, producing a precipitate enriched with the largest crystallites. We discarded the flocculate and collected the supernatant. Additional anhydrous ethanol was added into the supernatant to induce all remaining CQDs precipitate, and these were collected using centrifugation. Dispersion of the precipitate in toluene, and size-selective precipitation with ethanol was repeated again using the same procedure. Finally, the precipitate was collected and vacuum-dried for 30 min. Then, the resultant nanoparticles were dispersed in anhydrous toluene to a concentration of 150 mg mL^{-1}. The calculated overall yield of the size-selective precipitaion process to be 70 ± 5%.

Metal Halide Post-Treatment: A stock $CdCl_2$ precursor solution was prepared by dissolving 600 mg of $CdCl_2$ (3.2 mmol) and 66 mg (0.24 mmol) of tetradecylphosphonic acid (TDPA) in 10 mL of oleylamine, then heated to 100 °C for 1 h under nitrogen. The PbS CQD toluene solution was heated to 60 °C under vacuum for 30 min; then 1.0 mL of metal halide precursor was introduced into the reaction flask. A 6:1 Pb:Cd molar ratio was maintained during the treatment. The temperature was kept at 60 °C for 30 min and then cooled to room temperature. The nanocrystals were isolated by the addition of acetone followed by centrifugation. The nanocrystals were then purified by dispersion in toluene and reprecipitation with ethanol. Finally, they were re-dissolved in anhydrous octane at a concentration of 50 mg mL^{-1}.

Photovoltaic Device Fabrication: PbS CQD films were deposited using a layer-by-layer spin-casting process. For each layer, PbS CQDs in octane (50 mg mL^{-1}) were deposited on a substrate coated with fluorine-doped tin oxide (FTO) and TiO_2 and spin-cast at 2500 rpm for 10 s. A methanol solution containing 1%(v/v) mercaptopropionic acid (MPA) was dispensed on the substrate and spun after 3 s at 2500 rpm for 5 s. The film was rinsed twice with methanol to remove unbound ligands. The above process was repeated in a layer-by-layer fashion 10 times until the desired thickness was reached. The top electrodes were deposited using an Angstrom Engineering deposition system in an Innovative Technology glovebox. The contacts typically consisted of 10 nm of thermally evaporated molybdenum trioxide deposited at a rate of 0.2 Å s^{-1}, followed by electron-beam deposition of 50 nm of gold deposited at 0.4 Å s^{-1}, and finally 120 nm of thermally evaporated silver deposited at 1.0 Å s^{-1}.

Photovoltaic Performance Characterization: Current–voltage characteristics were measured using a Keithley 2400 source-meter in N_2 ambient conditions. The solar spectrum at AM1.5 was simulated to within class A specifications (less than 25% spectral mismatch) with a Xe lamp and filters (Solar Light Company Inc.) with a measured intensity at the sample surface of 100 mW cm^{-2}. The source intensity was measured using a Melles–Griot broadband power meter and a Thorlabs broadband power meter through a circular 0.049 cm^2 aperture at the position of the device and confirmed with a calibrated reference solar cell (Newport, Inc.). The accuracy of the power measurement was estimated to be ±5%.

GISAXS: GISAXS measurements were performed on Beamline 06ID-1 (HXMA) at the Canadian Light Source. Monochromatic light with a wavelength of 1.23984 Å (10 keV) was used. A Pilatus 1M detector, a CMOS hybrid-pixel CCD camera with a pixel size of 172 mm × 172 mm and a total of 981 × 1043 pixels with a 20-bit dynamical range per pixel, was used to record the scattering patterns. The typical readout time per image was <3.6 ms. The images were dark-current-corrected, distortion-corrected, and flat-field-corrected by the acquisition software. Using a silver behenate powder standard, the sample-to-detector distance was determined to be 1350.74 mm. The angle of incidence of the X-ray beam was varied between 0.02 and 0.158. Typical exposure times ranged from 20 to 300 s. All three films showed a primarily ring-like GISAXS patterns. We plotted azimuthally integrated intensity profiles and used Gaussian fitting plus an exponential background to determine the location of the scattering rings at $q \approx 0.2$ Å $^{-1}$. Conversion to real-space coordinates gave average center-to-center nanocrystal spacings of 5.5, 5.2, and 5.0 nm.

XPS Measurements: The surface elements and chemical states of the PbS CQD films were analyzed using X-ray photoelectron spectroscopy (XPS) (PHI-5500). A monochromated Al K radiation source (1486.7 eV) was used to excite photoelectrons in an ultrahigh vacuum atmosphere at ca. 10^{-9} Torr. The binding energy scale was calibrated using the Au 4f 7/2 peak at 83.98 eV and the Cu 2p 3/2 peak of sputter-cleaned Cu at 932.67 eV.

Photoluminescence Quantum-Efficiency Measurements: The PLQE was measured by mounting a small amount of CQD solution in a fiber-coupled integrating sphere. A 640 nm diode laser was used to excite the sample, and the photoluminescence and laser signals were collected using near-infrared- and visible-wavelength-range spectrometers, respectively. The PLQE was calculated by taking the integrated difference between the directly excited and indirectly excited photoluminescence photon signals divided by the integrated difference between the direct pump and indirect pump laser photon signals.

Supporting Information

Supporting Information is available from the Wiley Online Library or from the author.

Acknowledgements

This publication is based in part on work supported by Award KUS-11–009–21, made by King Abdullah University of Science and Technology

(KAUST), by the Ontario Research Fund Research Excellence Program, and by the Natural Sciences and Engineering Research Council (NSERC) of Canada. The authors thank Angstrom Engineering and Innovative Technology for useful discussions regarding material deposition methods and control of the glovebox environment, respectively. The research described in this paper was performed at the Canadian Light Source, which is funded by the Canada Foundation for Innovation, the Natural Sciences and Engineering Research Council of Canada, the National Research Council Canada, the Canadian Institutes of Health Research, the Government of Saskatchewan, Western Economic Diversification Canada, and the University of Saskatchewan. The authors would like to acknowledge the technical assistance and scientific guidance of C. Y. Kim, E. Palmiano, R. Wolowiec, and D. Kopilovic.

Received: December 1, 2013
Revised: January 16, 2014
Published online: March 21, 2014

[1] E. H. Sargent, *Nat. Photonics* **2012**, *6*, 133.
[2] M. Grätzel, R. A. J. Janssen, D. B. Mitzi, E. H. Sargent, *Nature* **2012**, *488*, 304.
[3] O. E. Semonin, J. M. Luther, S. Choi, Hsiang-Yu. Chem, J. Gao, A. J. Nozik, M. Beard, *Science* **2011**, *334*, 1530.
[4] I. J. Karmer, E. H. Sargent, *ACS Nano* **2011**, *5*, 8506.
[5] S. A. McDonald, G. Konstantatos, S. Zhang, P.W. Cyr, E. J. D. Klem, L. Levina, E. H. Sargent, *Nat. Mater.* **2005**, *4*, 138.
[6] A. H. Ip, S. M. Thon, S. Hoogland, O. Voznyy, D. Zhitomirsky, R. Debnath, L. Levina, L. R. Rollny, G. H. Carey, A. Fischer, K. W. Kemp, I. J. Kramer, Z. Ning, A. J. Labelle, K. W. Chou, A. Amassian, E. H. Sargent, *Nat. Nanotechnol.* **2012**, *7*, 577.
[7] M. Yuan, D. Zhitomirsky, V. Adinolfi, O. Voznyy, K. W. Kemp, Z. Ning, X. Lan, J. Xu, J. Y. Kim, H. Dong, E. H. Sargent, *Adv. Mater.* **2013**, *25*, 5586.
[8] I. J. Karmer, E. H. Sargent, *Chem. Rev.* **2014**, *114*, 863.
[9] X. Wang, G. I. Koleilat, J. Tang, H. Liu, I. J. Kramer, R. Debnath, L. Brzozowski, D. A. R. Barkhouse, L. Levina, S. Hoogland, E. H. Sargent, *Nat. Photonics* **2011**, *5*, 480.
[10] G. I. Koleilat, X. Wang, A. J. Labelle, A. H. Ip, G. H. Carey, A. Fischer, L. Levina, L. Brzozowski, E. H. Sargent, *Nano Lett.* **2011**, *11*, 5173.
[11] I. Moreels, Y. Justo, B. D. Geyter, K. Haustraete, J. C. Martins, Z. Hens, *ACS Nano* **2011**, *5*, 2004.
[12] M. A. Hines, G. D. Scholes, *Adv. Mater.* **2003**, *15*, 1844.
[13] J. Tang, D. A. R. Barkhouse, X. Wang, R. Debnath, R. Wolowiec, E. Palmiano, L. Levina, A. G. Pattantyus-Abraham, D. Jamakosmanovic, E. H. Sargent, *ACS Nano* **2010**, *4*, 869.
[14] J. W. Thomson, K , Nagashima, P. M. Macdonald, G. A. Ozin, *J. Am. Chem. Soc.* **2011**, *133*, 5036.
[15] L. Cademartiri, J. Bertolotti, R. Sapienza, D. S.Wiersma, G. von Freymann, G. A. Ozin, *J. Phys. Chem. B.* **2006**, *110*, 671.
[16] L. Cademartiri, E. Montanarim, G. Calestani, A. Migliori, A. Guagliardi, G. A. Ozin, *J. Am. Chem. Soc.* **2006**, *128*, 10337.
[17] I. Moreels, K. Lambert, D. Smeets, D. D. Muynck, T. Nollet, J. C. Martins, F. Vanhaecke, A. Vantomme, C. Delerue, G. Allan, Z. Hens, *ACS Nano* **2009**, *3*, 3023.
[18] D. Zhitomirsky, O. Voznyy, S. Hoogland, E. H. Sargent, *ACS Nano* **2013**, *7*, 5282.
[19] J. Tang, K. W. Kemp, S. Hoogland, K. S. Jeong, H. Liu, L. Levinal, M. Furukawa, X. Wang, R. Debnath, D. Cha, K. Chous, A. Fischer, A. Amassians, J. B. Asbury, E. H. Sargent, *Nat. Mater.* **2011**, *10*, 765.
[20] O. Voznyy, S. M. Thon, A. H. Ip, E. H. Sargent, *J. Phys. Chem. Lett.* **2013**, *4*, 987–992.
[21] A. G. Pattantyus-Abraham, I. J. Kramer, A. R. Barkhouse, X. Wang, G. Konstantatos, R. Debnath, L. Levina, I. Raabe, M. K. Nazeeruddin, M. Gratzel, E. H. Sargent, *ACS Nano* **2010**, *4*, 3374.
[22] C. Galland, Y. Ghosh, A. Steinbruck, J. A. Hollingsworth, H. Htoon, V. I. Klimov, *Nat. Commun.* **2012**, *3*, 908.
[23] S. M. Thon, A. H. Ip, O. Voznyy, L. Levina, K. W. Kemp, G. H. Carey, S. Masala, E. H. Sargent, *ACS Nano* **2013**, *7*, 7680.
[24] K. S. Jeong, J. Tang, H. Liu, J. Kim, A. W. Schaefer, K. Kemp, L. Levina, X. Wang, S. Hoogland, R. Debnath, L. Brzozowski, E. H. Sargent, J. B. Asbury, *ACS Nano* **2012**, *6*, 89.
[25] B. C. O'Regan, S. Scully, A. C. Mayer, E. Palomares, J. Durrant, *J. Phys. Chem. B* **2005**, *109*, 4616.
[26] C. G. Shuttle, B. O'Regan, A. M. Ballantyne, J. Nelson, D. D. C. Bradley, J. de Mello, J. R. Durrant, *Appl. Phys. Lett.* **2008**, *92*, 093311.
[27] Z. Li, F. Gao, N. C. Greenham, C. R. McNeill, *Adv. Funct. Mater.* **2011**, *21*, 1419.
[28] D. Zhitomirsky, I. J. Karmer, A. J. Labelle, A. Fischer, R. Debnath, J. Pan, O. M. Bakr, E. H. Sargent, *Nano. Lett.* **2012**, *12*, 1007.
[29] V. I. Klimov, A. A. Mikhailovsky, S. Xu, A. Malko, J. A. Hollingsworth, C. A. Leatherdale, H.-J. Eisler, M. G. Bawendi, *Science* **2000**, *290*, 314.
[30] J. S. Owen, J. Park, P.-E. Trudeau, A. P. Alivisatos, *J. Am. Chem. Soc.* **2008**, *130*, 12279.
[31] W. K. Bae, J. Joo, L. A. Padilha, J. Won, D. C. Lee, Q. Lin, W. Koh, H. Luo, V. I. Klimov, J. M. Pietryga, *J. Am. Chem. Soc.* **2012**, *134*, 20160.
[32] C. B. Murray, D. J. Norris, M. G. Bawendi, *J. Am. Chem. Soc.* **1993**, *115*, 8706.